Dynamic compressive strength properties of aluminium foams. Part I—experimental data and observations

P.J. Tan, S.R. Reid*, J.J. Harrigan, Z. Zou, S. Li

School of Mechanical, Aerospace and Civil Engineering, The University of Manchester, P.O. Box 88, Sackville Street, Manchester M60 1QD, UK

Abstract

This study of the dynamic compressive strength properties of metal foams is in two parts. Part I presents data from an extensive experimental study of closed-cell Hydro/Cymat aluminium foam, which elucidates a number of key issues and phenomena. Part II focuses on modelling issues.

The dynamic compressive response of the foam was investigated using a direct-impact technique for a range of velocities from 10 to $210 \, \text{ms}^{-1}$. Elastic wave dispersion and attenuation in the pressure bar was corrected using a deconvolution technique.

A new method of locating the point of densification in the nominal stress–strain curves of the foam is proposed, which provides a consistent framework for the definition of the plateau stress and the densification strain, both essential parameters of the 'shock' model in Part II. Data for the uniaxial, plastic collapse and plateau stresses are presented for two different average cell sizes of approximately 4 and 14 mm. They show that the plastic collapse strength of the foam changes significantly with compression rate. This phenomenon is discussed, and the distinctive roles of microinertia and 'shock' formation are described. The effects of compression rates on the initiation, development and distribution of cell crushing are also examined. Tests were carried out to examine the effects of density gradient and specimen gauge length at different rates of compression and the results are discussed. The origin of the conflicting conclusions in the literature on the correlation between nominal strain rate $\dot{\varepsilon}$ (ratio

*Corresponding author. Tel.: +44 161 200 3848; fax: +44 161 200 3849.
E-mail address: steve.reid@manchester.ac.uk (S.R. Reid).

of the impact velocity V_i to the initial gauge length l_o of the specimen) and the dynamic strength of aluminium alloy foams is identified and explained.

1. Introduction

When closed-cell metal foams are compressed, work is done in bending and stretching the cell walls and in compressing the gas within the cells, if the membranes that form the cell faces do not rupture during compression (Gibson and Ashby, 1997). The propensity of aluminium foam to undergo gross 'plastic' deformation at an almost constant nominal load with large strokes makes it attractive for absorbing the energy of impact or impulsive loads in packaging applications, crash situations and for blast protection.[1] Therefore, an understanding of how the topological arrangement of the cell structure in the foam and the material behaviour of the solid phase, relate to the strength properties of a foam and its macroscopic response at different loading rates is a prerequisite to their successful implementation. High-rate loading experiments also provide the critical data required for developing predictive constitutive models for metal foams.

The literature contains conflicting, and sometimes confusing, conclusions on the correlation between compression rate (particularly when referred to the nominal engineering strain rate $\dot{\varepsilon} \equiv V_i/l_o$, where V_i is the impact velocity and l_o the initial gauge length of the specimen) and the dynamic strength of aluminium-based foams. Kenny (1996) reported that the specific energy absorption of Alcan[2] foams is independent of compression rate from 10^{-3} to $10^3 \, s^{-1}$ (an impact velocity of $10 \, ms^{-1}$ corresponding to a nominal compression rate of $10^3 \, s^{-1}$ in his tests); similarly, for Duocel foams (Lankford and Danneman, 1998). The study by Deshpande and Fleck (2000) on Alulight and Duocel foams showed that their plateau strength remains rate insensitive up to a nominal strain rate of $5 \times 10^3 \, s^{-1}$ (corresponding to an impact velocity of $50 \, ms^{-1}$). This contradicts the results of Mukai et al. (1999) who reported a 50–100% enhancement of the quasi-static plateau strength in closed-cell Alporas foams for compression rates greater than $10^3 \, s^{-1}$ (corresponding to an impact velocity of $6 \, ms^{-1}$). The confusion relates to several factors including misunderstanding the underlying mechanisms responsible for strength enhancement, inconsistencies in the definition of key material parameters such as the strain at which densification occurs, the definition of the plateau stress and, partly, to the

---

[1]Some studies have suggested that a protective foam layer could have the deleterious effect of enhancing, rather than attenuating, the blast wave transmitted to the face of the object to be protected (see, for example, Skews et al., 1993; Nesterenko, 2001). This remains an open problem requiring further investigations and validation, which is beyond the scope of the present paper.

[2]Alcan, Duocel, Alulight and Alporas are product names of various aluminium-based foams (open and closed cell) by different manufacturers. See Ashby et al. (2000) for information.

choice of experimental technique. There is, therefore, a need to clarify the underlying inconsistencies in the literature on the response of metal foams to dynamic loads.

In this paper, the response of metal foams to dynamic loads is investigated for Hydro/Cymat[3] foam specimens using a direct-impact technique (Reid and Peng, 1997). The measured force pulses were corrected for elastic wave dispersion and attenuation in the pressure bar load cell and for the presence of a small anvil using a force-deconvolution method. Experimental data obtained from 45 mm diameter specimens including the uniaxial, plastic collapse and plateau stresses are presented for two different average cell sizes (diameters) of approximately 4 and 14 mm. Both cell sizes exhibit significant enhancement of their plastic collapse stresses (defined in Section 3.1.2) for the entire range of velocity from 10 to 210 ms^{-1}. The dynamic plateau stresses, on the other hand, are insensitive to impact velocity below values of $\sim$50 and $\sim$80 ms^{-1} for the *large* (14 mm) and *small* (4 mm) cell specimens, respectively. Overall shortening of the specimen is achieved by the accumulation of discrete, non-contiguous bands of crushed cells. However, beyond a critical impact velocity of approximately 42 ms^{-1} (*large* cell specimens) or 108 ms^{-1} (*small* cell specimens), cell crushing occurs sequentially, in a planar manner, along the axis of the specimen from the impact-end and the crushing wave front has 'shock-type'[4] characteristics.

The increase in the energy absorption capacity of the foam, in the 'shock-dominated' loading regime is highlighted. It is also shown that the data have certain features in common with those of cellular systems constructed from simple engineering components, such as bars, plates and tubes (see review by Reid et al., 1993). Numerical simulations of the in-plane compression of honeycombs, e.g. Papka and Kyriakides (1994), Hönig and Stronge (2002) and Ruan et al. (2003) have established an understanding of the mechanisms that underpin much of our later discussion of the dynamic properties of foams.

Finally, tests were carried out to examine the effects of specimen size at different compression rates. They help clarify two related issues: first, the existence of an intrinsic specimen length scale; and second the correlation between compression rates and dynamic strength. The experimental data described herein will be used to validate the predictions of a one-dimensional (1D) 'steady-shock' model in the companion paper.[5]

---

[3]Cymat and Norsk Hydro had merged their aluminium foam process technologies with the former having acquired all of Norsk Hydro's intellectual property and production assets related to aluminium foam production.

[4]Note that herein the term 'shock' wave describes the motion of an interface, measured with reference to the initial undeformed configuration of the specimen, which separates crushed and uncrushed cells, during a sequential cell-crushing process. This is an inertial phenomenon often associated with the high velocity compression of cellular materials and structures (Reid et al., 1993). It is not the classical shock wave studied by fluid mechanicists and shock physicists. Rather, the response exhibits 'shock-type' characteristics and the basic jump conditions can equally be used to describe the dynamical conditions across the crushing wave, or 'shock', front. Terms such as compaction or densification waves could be used equally.

[5]Tan et al. (2005). Part II—'Shock' theory and comparison with experimental data and numerical models. J. Mech. Phys. Solids, in press.

2. Description of material, experimental set-up and force measurement technique

2.1. Material description

The solid phase (cell wall) material was an Al–Si(7–9%)–Mg(0.5–1%) alloy. It has a density (ρ_s) of 2730 kg m^{-3}, Young's modulus (E_s) of 70 GPa and yield strength (σ_{ys}) of 185 MPa (Hanssen, 2000). The three mutually perpendicular principal directions in a typical foam panel, viz. *casting* (x), *transverse* (y) and *gravity* (z), are shown in Fig. 1. To characterise their directional properties, circular cylinders with their axes in either the y- or the z-directions—their strength differences are greatest between these two directions—were cut from a panel by spark machining. All the cylindrical specimens had equal gauge length l_o and diameter d_o of approximately 45 mm unless stated otherwise.

The specimens are comprised of approximately equiaxed, closed-polyhedral cells with about 10–15 faces. Each cell has an approximate diameter of $d_c = 2 \cdot \sqrt{A_c/\pi}$, where A_c is the projected cell area onto a plane. Fig. 2 shows the frequency of occurrence, $f(d_c)$, of a given cell diameter d_c, against d_c, in two y-axis specimens with different average cell sizes. The average cell diameter in a specimen is given by (Gibson and Ashby, 1997)

$$\bar{d} = \int_0^\infty d_c \cdot f(d_c) d(d_c) \tag{1}$$

and the cell diameter dispersion (standard deviation) is

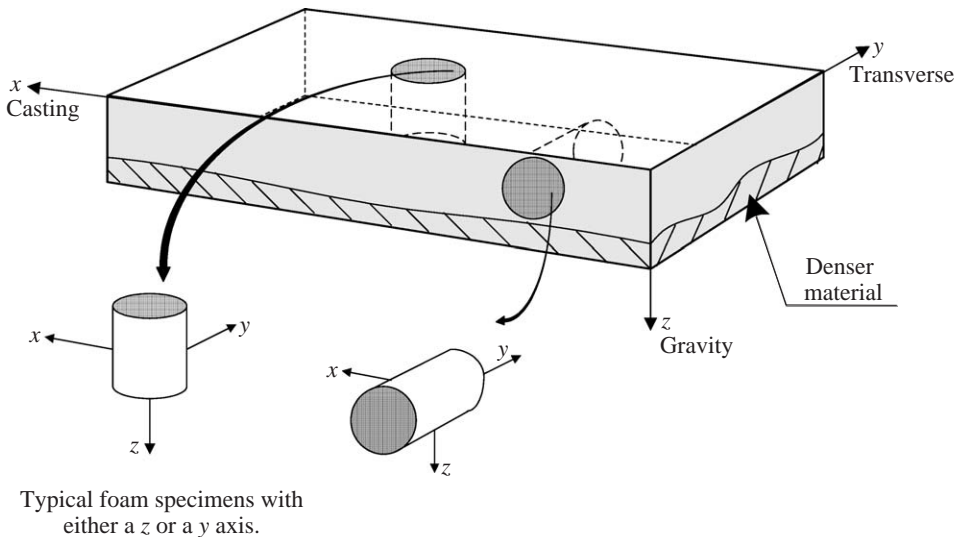$$\mu_{\bar{d}} = \int_0^\infty (d_c - \bar{d})^2 \cdot f(d_c) d(d_c). \tag{2}$$

Fig. 1. Reference system for a typical Hydro/Cymat foam panel.
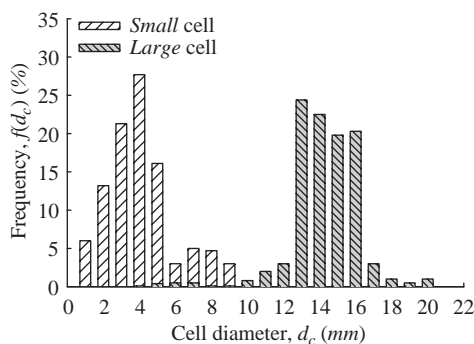
Fig. 2. Cell diameter distribution in typical *small* and *large* cell *y*-axis specimens.

Table 1
Characterisation chart for Hydro/Cymat foams

Material	AlSi8Mg (base alloy),	SiC (particle type)
Density, ρ_0 (kg m^{-3})	187–512	107–346
Open or closed cells	Closed	
Mean cell diameter, $\bar{d}$ (mm)	4	14
	(*small*-cell)	(*large*-cell)
Standard deviation of $\bar{d}$, $\mu_{\bar{d}}$ (mm)	3.51	3.56
Largest principal cell dimension, $\bar{L}_y$ (mm)	4.12	15.96
Smallest principal cell dimension, $\bar{L}_z$ (mm)	3.66	13.25
Intermediate principal cell dimension, $\bar{L}_x$ (mm)	3.87	14.04
Shape anisotropy ratios, R_{yz}, R_{yx}	$R_{yz} = 1.13$	$R_{yz} = 1.20$
	$R_{yx} = 1.06$	$R_{yx} = 1.14$
Other specific features	Non-uniform density distribution along the *z*-axis (see Fig. 3)	

In Fig. 2, the two average cell sizes are approximately 14 and 4 mm; for brevity they will be referred to as *large* cell and *small* cell specimens, respectively, hereinafter. The former has greater cell diameter dispersion. With our choice of dimensions, the *small* and *large* cell specimens have more than 10 cells and approximately 3–5 cells, respectively, in the transverse circular plane perpendicular to the direction of loading. It is anticipated that the properties of the latter are likely to be affected by size effects (Andrews et al., 2001) and the reasons for studying these specimens will be given later. Primarily due to the manufacturing process, cylinders of the *large* and *small* cell specimens have average densities ρ_o that range from 107 to 346 and 187 to 512 kg m^{-3}, respectively. Common cell morphological defects, such as missing cells, non-uniform cell wall thickness, fractured cell-walls, cell-size variations, misalignment of cell walls and cell wall waviness, are present in all our specimens (Chen et al., 1999), being most severe in the *large* cell specimens. A detailed analysis of the cell morphology is beyond the scope of this work; nonetheless, some of the more important geometrical characteristics are listed in Table 1.

2.2. Directional differences

The density (normalised by the density of the cell wall material ρ_s) distributions along the z-axis and the y-axis of two typical *small* cell specimens are shown in Figs. 3a and b, respectively. The former has cell edges (and also their cell faces) that tend to greater thickness in the positive z-direction. This is due to foam drifts caused by alternate impellers rotating in opposite directions during foaming (Harte and Nichol, 2001). Specimens with axes aligned along (in) the z-direction are non-homogeneous, with spatial variations of density that have an approximate
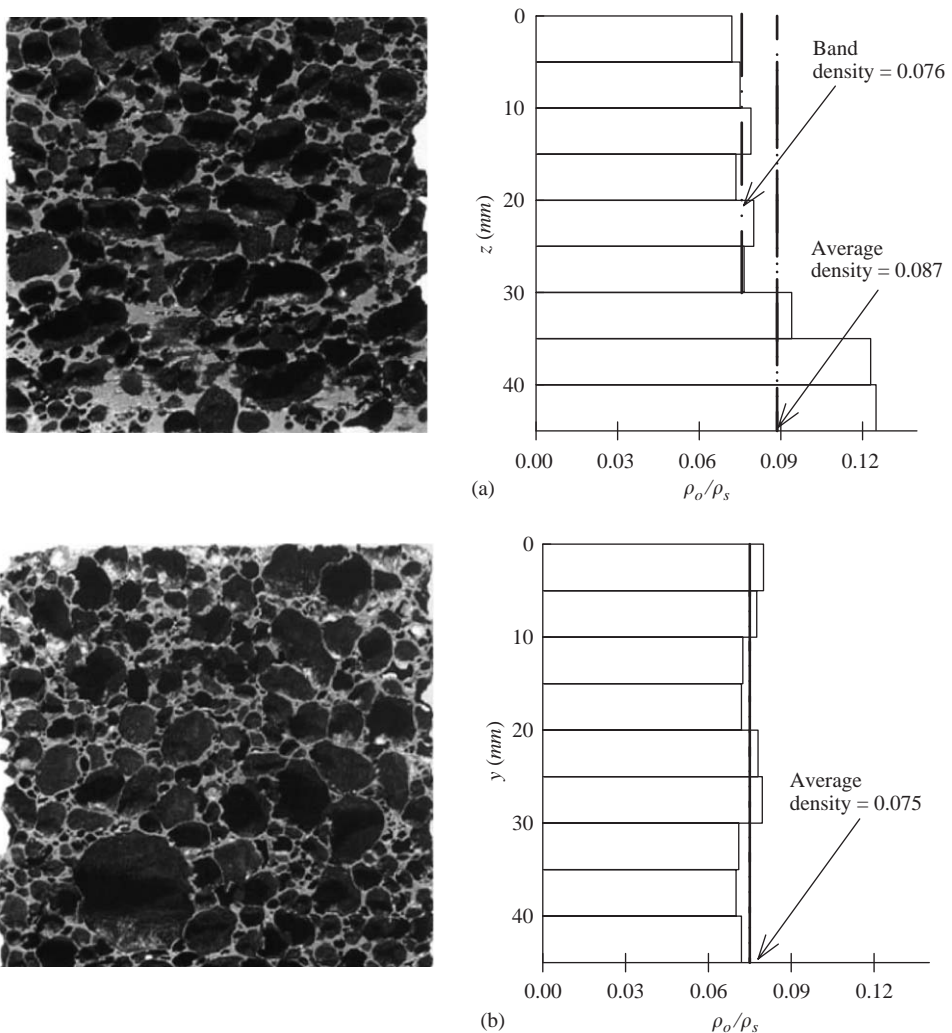

Fig. 3. Density distribution in two *small* cell specimens in the (a) z- and the (b) y-direction. Both specimens ($l_o = d_o = 45$ mm) were sectioned along their respective diametrical mid-plane.

step-distribution. In contrast, the density distributions in specimens aligned in the
y-direction are relatively uniform. The same trend is also observed for the *large*
cell specimens. If the band of cells with greater wall thickness is parallel to the
loading axis, it acts to reduce the effects of imperfections by strengthening and
stabilising the specimen during compression (Chastel et al., 1999). For this reason
the cutting of cylindrical specimens along the y-axis was carried out in a manner
in which the denser material at the base of a foam slab is avoided—see schematic
in Fig. 1b.

   Macroscopic anisotropy due to cell elongation in the foam is characterised by the
shape anisotropy ratios, $R_{ij} = \bar{L}_i/\bar{L}_j$ and $R_{ik} = \bar{L}_i/\bar{L}_k$, where $\bar{L}_i$ is the largest
principal cell dimension and the subscripts i, j and k refer to the three principal
directions in Fig. 1 (Gibson and Ashby, 1997). The shape anisotropy ratios for the
two average cell sizes are given in Table 1. In both cases, the slightly elongated cells
have their largest principal dimension in the *transverse* (y) direction. The data for the
small cell specimen suggests that the mean cell diameter in the y-direction is
marginally larger by factors of $R_{yz} = 1.13$ and $R_{yx} = 1.06$ compared to those in the
z-and the x-directions, respectively. The same can also be said of the *large* cell
specimens but with different factors.

2.3. Force measurement techniques and experimental set-up

   Two common experimental techniques used in the high-rate testing of metal foams
are the split Hopkinson pressure bar (SHPB) ($200 < \dot{\varepsilon} < 10^4\,\mathrm{s}^{-1}$) and direct-impact
($10^3 < \dot{\varepsilon} < 10^5\,\mathrm{s}^{-1}$) tests. A comprehensive review of each technique is unwarranted;
however, their limitations and important considerations in the design of test
specimens are considered next. Hereinafter, the terms incident/input and transmitter/
output have their usual meanings in the context of a standard SHPB set-up while
only the latter is used in a direct-impact set-up.

2.3.1. Split Hopkinson pressure bar versus direct-impact techniques

   Both techniques utilise strain-gauged, cylindrical pressure bar(s) as the basis for a
mechanical method of measuring stress (or, more correctly, strain) wave pulses
generated by impact. The sensitivity of the pressure bar is determined by the
properties of the material of the bar (density, ρ_b), the type of strain gauge used and
the characteristics of the associated instrumentations. Although the bar can be made
of any solid material, the elastic wave impedance ($\equiv \rho_b C_e$ where C_e is the elastic
wave speed) of the material to be tested usually dictates the choice. Imagine a
homogeneous foam specimen (one aligned with the y-axis) idealised as a 1D chain of
particles of equal mass m ($= \rho_o A_o \bar{d}$) that are interconnected by identical, massless
linear elastic springs of stiffness e ($= E_f A_o/\bar{d}$), where E_f is Young's modulus of the
foam and A_o is the cross sectional area of the undeformed specimen. If dispersion
effects and wave attenuation are neglected then the speed of an elastic wave (plane
stress) propagating in this chain is (Brillouin, 1946)

$$C_e = \bar{d} \cdot \sqrt{e/m} = \sqrt{(E_f/\rho_o)}. \tag{3}$$

Using Eq. (3) the wave impedance of a typical *small* cell specimen ($\rho_o = 350\,\mathrm{kg\,m^{-3}}$ and $E_f \approx 1.6\,\mathrm{GPa}$) is estimated to be $\sim 0.75 \times 10^6\,\mathrm{kg\,m^{-2}\,s^{-1}}$—two orders of magnitude lower by comparison with that of standard steel ($\sim 40 \times 10^6\,\mathrm{kg\,m^{-2}\,s^{-1}}$). The high impedance mismatch suggests that a bar with lower acoustic impedance is needed for the SHPB test. Otherwise, the forces at the specimen-input bar interface cannot be resolved accurately—the incident and reflected force pulses being almost identical and so essentially cancelling each other. However one of the difficulties with, for example, polymer bars, such as PMMA, is the need to employ complex geometry-dependent viscoelastic model analysis of the pressure bar signals to deduce the specimen behaviour. This contrasts with the straightforward data reduction if steel bars are used. If, on the other hand, a linear elastic data reduction is used with polymer bars, errors of up to 52% can be expected (Wang et al., 1994). Finally, it is noted that the technique used by Deshpande and Fleck (2000) to justify a linear elastic data reduction did not consider the critical effects of signal frequencies upon wave attenuation and dispersion (Bacon, 1998, 1999). Therefore, their results must be interpreted with care.

There are also important considerations in the design of the test specimens for a SHPB test. The errors due to the radial and the longitudinal inertia of the specimen have to be minimised by choosing a specimen aspect ratio of (Davies and Hunter, 1963)

$$d_o/l_o = 2/\sqrt{3.v_f}, \tag{4}$$

where v_f is the Poisson's ratio: typically between 0.31 and 0.34 for Hydro/Cymat foams (Ashby et al., 2000). The errors due to friction at the specimen-pressure bar interfaces must be minimised by reducing the areal mismatch between specimen and bars. A short specimen length is also required for rapid 'ring-up' (often described as attaining equilibrium) to a uniform uniaxial stress state. If the deformation of the specimen follows the Taylor–von Karman theory, then the minimum 'ring-up' time is given by Davies and Hunter (1963) as

$$t \geqslant \pi \cdot l_o \sqrt{\rho_o/(\partial\sigma/\partial\varepsilon)}, \tag{5}$$

where $\partial\sigma/\partial\varepsilon$ is the tangent modulus of the specimen's true stress–strain curve. Although, a shorter specimen achieves uniform stress much quicker (Eq. (5)), l_o cannot be reduced without a concomitant reduction in both the specimen (Eq. 4)) and pressure bar diameters. A minimum diameter ratio of $d_o/\bar{d} \geqslant 5$ for a foam test specimen is necessary to avoid size effect (Andrews et al., 2001). Lastly, the specimen gauge length has to be greater than the length scale that defines the continuum limit of the foam (this is discussed in Section 3.2.3). It is not often possible for the specimen to satisfy all of the above criteria and its final design is usually a compromise.

In a SHPB test, the dynamic stress–strain response is deduced on the premise that there is internal force equilibrium and uniform deformation in the test specimen. Since localisation is a distinctive feature of the deformation of metal foams, the requirement for uniform deformation of the test specimen in a SHPB test is, strictly

speaking, not met initially or at all unless l_o is $O(\bar{d})$. Therefore, the results of a SHPB test on metal foams must be interpreted with care.

In a direct-impact test, the test specimen is attached to one end of the striker bar (better termed, in this case, the backing mass) and this end is projected so that it impacts the output bar directly. The transmitted wave signal gives the variation of the crushing force (or nominal stress when normalised by A_o) with time. Although this technique increases the maximum loading rate achievable it, too, poses several difficulties. Neither the nominal strain nor the nominal strain rate in the specimen can be evaluated without an incident bar. However, this limitation can be overcome (see Gorham et al., 1992). A constant strain rate is not achieved because the specimen lacks internal force equilibrium. Therefore, the ratio V_i/l_o is, at best, an overestimate of the actual strain rate in the specimen; nevertheless, it provides a useful value for test design. Just as with the SHPB technique, specimens must also be sized to avoid size effect and specimen length effect. Finally, whilst the direct impact test as described above can be used to measure the force pulse behind the deformation front, the pulse exerted at the support surface of the specimen can be measured by placing the specimen at the end of the output bar and striking it with the input bar. The direct-impact technique is advocated for metal foam testing because, unlike a SHPB test, no assumptions regarding the deformation in the test specimens need to be made.

2.3.2. Apparatus and experimental set-up

A thick-walled, tool-steel chamber of 45 mm inner diameter (see Fig. 4) was used to prevent the premature break-up of the specimens by buckling and/or shear banding during the quasi-static and the dynamic compression tests. Fig. 5 shows typical quasi-static stress–strain curves for *small* cell specimens (at 16% relative density) with (uniaxial strain) and without (uniaxial stress) the radial constraint. Significant differences between their compressive responses are only observed for the densification régime, i.e. after the point of densification (defined later on). Because the present study is concerned with the strength properties defined in the pre-densification régime (compare the data given in Fig. 5), it is concluded that the radial
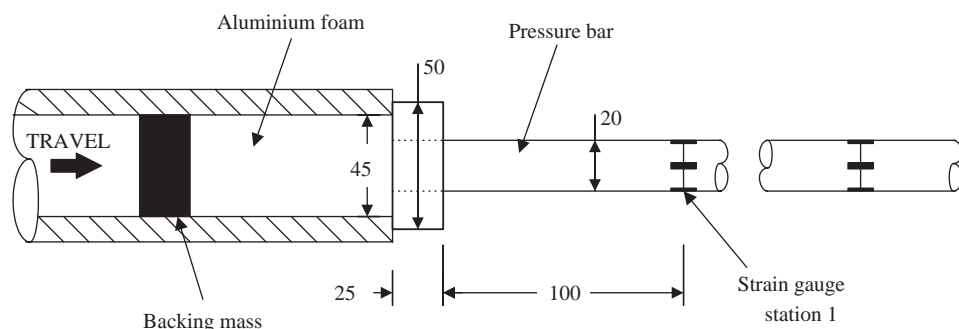

Fig. 4. Schematic of experimental set-up for direct impact testing of aluminium foam projectiles.
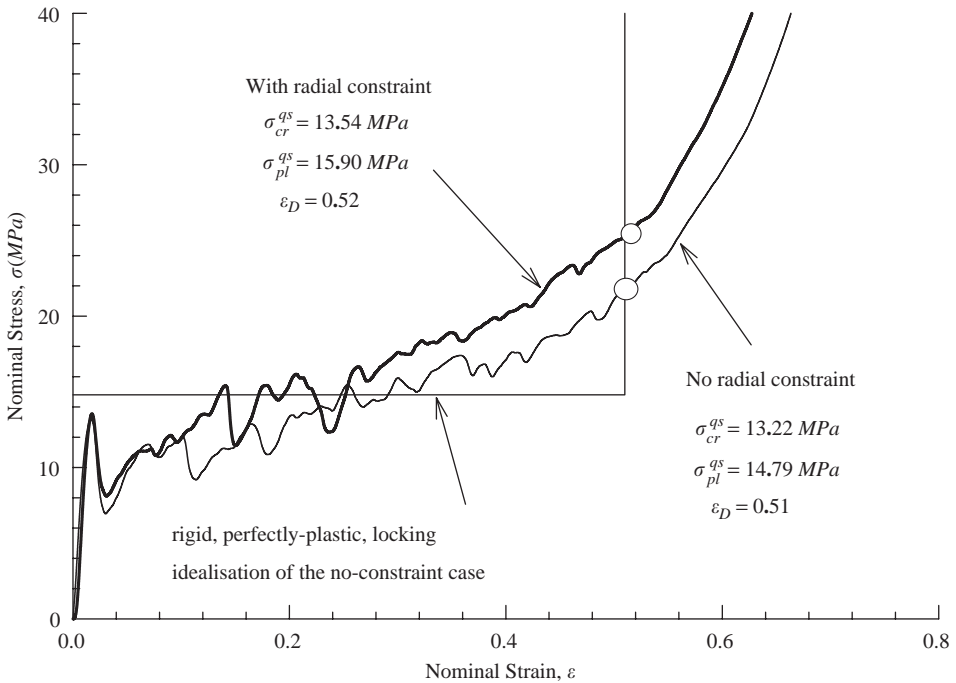
Fig. 5. Quasi-static stress–strain curves of specimens (16% relative density) with and without a radial constraint. The circle marks the point of densification in each curve. The r-p-p-l idealisation of the stress–strain curve for the case without a radial constraint is plotted.

confinement had little effect. Likewise, for specimens subjected to dynamic compression. Radford et al. (2005) recently presented a similar comparison for Alporas foam and the same conclusion could also be reached with their data. In order to reduce the effect of frictional restraint, the contact surfaces between the specimen and pressure bar/chamber were lubricated with PTFE spray.

Quasi-static testing of the specimens was carried out on an Instron-4507 testing machine under room temperature conditions (18 °C, 55% relative humidity) at a constant displacement rate $\dot{\delta}$ of 45 μm s^{-1}. A direct-impact technique was used for the dynamic testing of the foam specimens. Because a steel output bar was chosen (due to the more straightforward data reduction), modifications to the original experimental set-up—described in detail by Reid and Peng (1997) — were needed to increase the signal-to-noise ratio of the strain gauge measurements (the location of the strain gauges on the bar is shown in Fig. 4). This was achieved in two ways. The diameter of the pressure bar was reduced to 20 mm. This increased the strength of the signal. Also the upper frequency limit of the amplifier ('Fylde' H359-TA) was lowered to 160 kHz—this reduced the effects of high-frequency noise. Because the bar diameter used was then less than those of the specimens, the areal mismatch was dealt with by using an anvil of 50 mm outer diameter (similar to that used in

Harrigan et al., 1998a) which was shrink-fitted to one end of the bar (see Fig. 4). Both the bar and anvil were made of silver steel. A simple static calibration allowed the conversion of the strain gauge output signal to the corresponding force pulse. The gain of the amplifier was 500 and the bandwidth of the oscilloscope (LECROY) was set to its lowest value of 30 MHz.

An aluminium backing mass (with a diameter of ~45 mm) was attached to the rear (distal) end of each specimen (see Fig. 4). This has two purposes: it helped with the alignment of the specimen in the barrel of the pneumatic launcher; and it provided additional kinetic energy for specimen crushing. The biggest possible backing mass that is consistent with not yielding the pressure bar was chosen for each specimen. It is convenient to introduce a dimensionless mass ratio

$$M_r = M_b/M_f = 4M_b/\pi\rho_o l_o d_o^2, \tag{6}$$

where M_f and M_b are the mass of the specimen and backing mass, respectively. In general, a higher mass ratio is needed for complete crushing of the specimen at lower loading rates. Useful information is normally restricted to the first 800 μs of the force pulse—known as the bar transit time—because of signal reflection from the free end of the output bar. The bar transit time is determined by the properties of the material of the bar.

2.3.3. Deconvolution method for the indirect measurement of impact force

Inoue et al. (2001) described an inverse analysis using deconvolution to estimate the impact forces induced by a collision of two bodies of arbitrary shape. Dispersion of the elastic waves in the pressure bar due to 3D elastic wave propagation and the presence of the anvil effect the signal oscillations and cause a gradual increase in the rise time of the force pulse with propagation distance.

A time-dependent force pulse is a superposition of plane waves of many frequencies, each of which will travel at a different velocity when dispersion is present. If there is a linear mapping of the unknown force pulse $F_c(t)$, generated at the common plane of impact, onto $F_m(t)$, measured by the strain gauges, then they are related to each other according to the convolution or Faltung's theorem as follows: (Arfken and Weber, 1995)

$$F_m(t) = \int_0^\infty \Phi(t - \tau)F_c(\tau)\,d\tau, \tag{7}$$

where $\Phi(t - \tau)$ is an amplitude and phase modifying (transfer) function. The concept of causality is invoked requiring $\tau < t$ in Eq. (7) (Arfken and Weber, 1995). Taking the Laplace transform of the definite integral in Eq. (7) gives

$$\overline{F}_m(s) = \overline{\Phi}(s)\overline{F}_c(s). \tag{8}$$

The transfer function $\overline{\Phi}(s)$ is normally derived from a calibration experiment (Inoue et al., 2001).

Here, the approach by Harrigan et al. (1998b) was adopted and the transfer function was derived numerically using finite elements (*ABAQUS*) because of the practical difficulties of attaching strain gauges to foam projectiles. The pressure bar
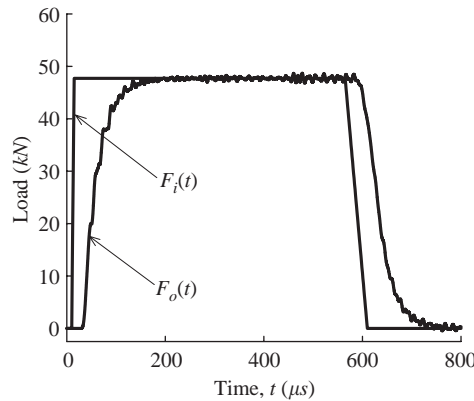
Fig. 6. The prediction by *ABAQUS* of the output force pulse $F_o(t)$, measured at strain gauge station 1, for a prescribed input force pulse $F_i(t)$, acting at the specimen-pressure bar interface (Harrigan and Reid, 1998b).

geometry, the material properties of the bar (including material damping), the boundary and support conditions were accurately specified and a mesh sensitivity study was made (see Harrigan et al., 1998b; Inoue et al., 2001). Fig. 6 shows the difference between the predicted response, $F_o(t)$, at strain gauge station 1, for a prescribed input force pulse $F_i(t)$, acting at the specimen-input bar interface, produced by *ABAQUS*. Accordingly, the transfer function (in the transform space) was

$$\overline{\Phi}(s) = \overline{F}_o(s)/\overline{F}_i(s). \tag{9}$$

Substituting Eq. (9) into Eq. (8), and applying the inverse Laplace transform, the unknown force pulse $F_c(t)$ at the point of impact is given by (Inoue et al., 2001)

$$F_c(t) = \frac{1}{2\pi i} \int_{\gamma-i\infty}^{\gamma+i\infty} [\overline{F}_i(s) \cdot \overline{F}_m(s)/\overline{F}_o(s)] \cdot e^{st} \, ds. \tag{10}$$

All the Laplace and inverse transformations were carried out numerically by fast Fourier transforms (see Inoue et al., 1992).

The force pulses were smoothed, in an 11-point moving average process, before they were corrected by deconvolution (see Harrigan et al., 1998b). Fig. 7 shows typical force pulses of a *small* and a *large* cell specimen before and after deconvolution. Unlike the former, the corrected force pulses of the *large* cell specimen fluctuated wildly. For the *small* cell specimens, noise contributions are typically less than 5.5% of the plateau force measured at an impact velocity of 13.44 ms^{-1}. Hence, any changes in $\overline{F}_m(s)$ are less significant after inversion as seen in Fig. 7a. By contrast, noise contributions are up to 60% of the plateau force in *large* cell specimens measured at impact velocities of $V_i \leqslant 20$ ms^{-1} (Fig. 7b). For these reasons, the measured force pulses of all the *large* cell specimens were not corrected by deconvolution in this study, rather the raw signals were used. It is also worth noting the significant modification to Phase I (see Section 3.2.1) of the deconvoluted
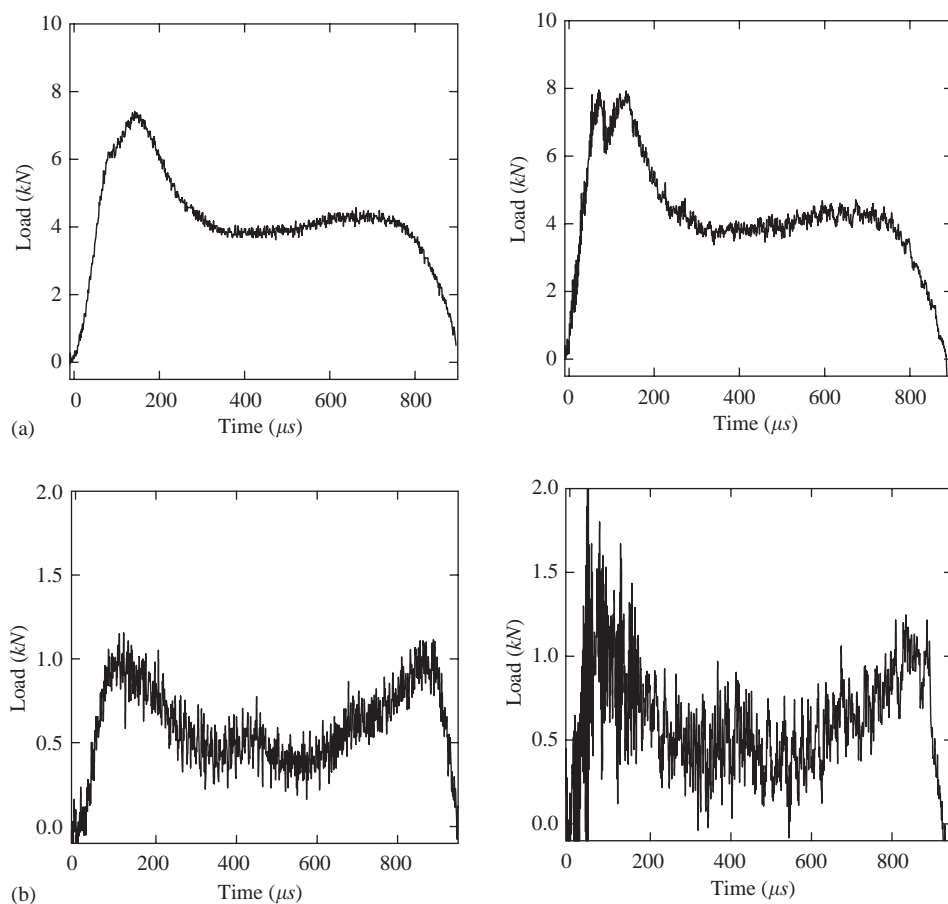
Fig. 7. Force pulse of a *small* and a *large* cell *y*-axis specimen before (left) and after (right) deconvolution (a) *small* cell specimen, $V_i = 13.44\,\text{ms}^{-1}$, $\rho_o/\rho_s = 0.122$, $M_r = 16.87$ and, (b) *large* cell specimen, $V_i = 12.01\,\text{ms}^{-1}$, $\rho_o/\rho_s = 0.0503$, $M_r = 56.94$.

force pulse (see Fig. 7a). By contrast, Phases II and III appear largely unaffected with only a noticeable increase in noise superimposed on the raw signal.

3. Results of experiments

3.1. Quasi-static compression

To illustrate the range of phenomena involved when closed-cell metal foam is compressed, the quasi-static response of Cymat/Hydro foams to uniaxial compression is briefly described first. This also provides a reference point for the subsequent discussion of the dynamic test data in Section 3.2.

3.1.1. Nominal stress–strain curves

Fig. 8 shows typical quasi-static compressive stress–strain curves for *small* and *large* cell specimens in the *y*- and the *z*-directions. All stress and strain measures are based on engineering stress and nominal strain definitions. Like those of other cellular solids, they show linear elasticity at low stresses followed by a 'plateau' region and then a régime of densification in which the stress rises steeply (Gibson and Ashby, 1997). These common features of the curves are described first. However it should be noted at this point that, whilst the detailed stress–strain curves are of
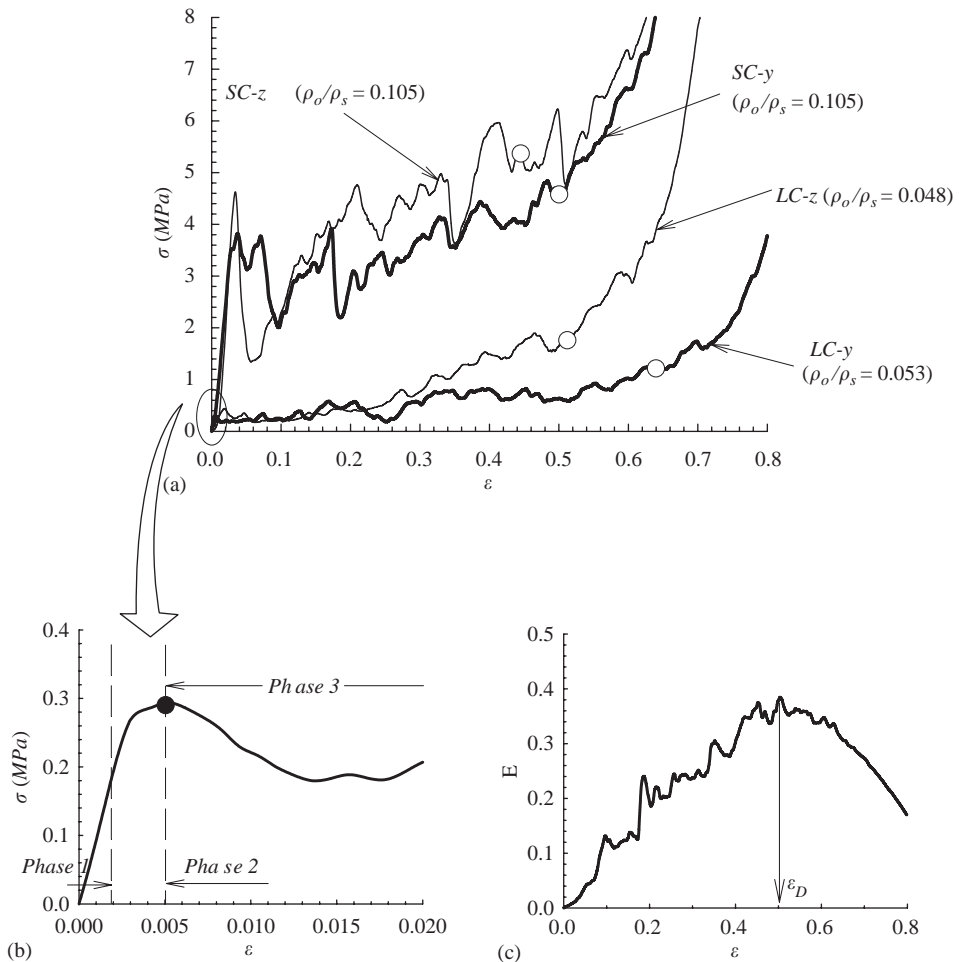

Fig. 8. (a) Typical nominal stress–strain curves of *small* cell (*SC*) and *large* cell (*LC*) specimens compressed along their *y* (thick line) and *z* (thin line) axes. The hollow circles mark their respective point of densification. (b) Three phases of early deformation response in the *large* cell foam with a *y*-axis (*LC-y*). A solid circle marks the plastic collapse stress. (c) Efficiency–strain curve for *SC* foam compressed along their *y*-axis (*SC-y*).

intrinsic interest, it is the objective of this section to provide a simplified description of the behaviour of the foam, according to the rigid-perfectly plastic-locking (r-p-p-l) idealisation in which the foam is characterised mainly by its plastic collapse stress σ_{cr}^{qs}, its plateau stress σ_{pl}^{qs} and its densification strain ε_D (see Fig. 5). These parameters are particularly useful in characterising the dynamic response of the foam, the focus of this paper and its companion. The material response in the densification régime is, by contrast, of lesser intrinsic interest when designing with foams for impact energy absorption.

The early response is divided into three phases—see Fig. 8b. Phase I corresponds to linear, elastic straining of the specimen through cell wall bending and cell face stretching (Gibson and Ashby, 1997). This occurs at small nominal strains. Further straining now causes the localised plastic deformation that has already developed around small domains of spatially correlated defects to spread and, eventually, coalesce to form bands (or layers) of deforming cells that advance across the specimen. Its cumulative effect is reflected in the non-linear, 'concave-upwards' response of the stress–strain curves (denoted by Phase 2). A stress (or load) drop accompanies the initiation of plastic collapse, at σ_{cr}^{qs}, in the weakest band of cells, which marks the beginning of Phase 3. This is analogous to the response of a Type II strut (see Calladine and English, 1984) to quasi-static compression. Data for their shape anisotropy ratios (Table 1) suggest that the load drop should be greater for compression in the y- than in the z-direction, but this is not consistently reflected in the curves of Fig. 8 because of variable geometry of the cell structure. The mode of cell collapse per se is too difficult to quantify, unlike for honeycombs under in-plane compression. Nonetheless, examination of partially crushed foam specimens suggests that the cells deform in a non-symmetric (shear-type) mode. Non-symmetric cell deformation leads to a decrease in elastic stiffness that results in a maximum load followed by a subsequent plastic loading path with a negative slope as seen in Fig. 8 (Papka and Kyriakides, 1994). When opposing walls of the cells in a collapsing band touch each other, the cells stiffen locally and this triggers the plastic collapse of a non-contiguous band of cells. Each band appears to develop a spacing of 3–4 mean cell diameters from each other— consistent with the results of surface deformation analysis by Bastawros et al. (2000). This is only seen in *small* cell specimens with a long gauge length. Otherwise, the crush bands intersect each other and are inclined at angles of approximately 25° to the loading axis. The process of discrete crush band multiplication is repeated, causing stress oscillations in the long 'plateau', though this exhibits gradual overall strain hardening. This region of the stress–strain curves continues until bands of collapsed cells permeate the entire specimen; thereafter, the cell wall material itself is compressed. These observations are broadly similar to the ones made by Bastawros et al. (2000).

There are, however, important differences between the curves shown in Fig. 8. First consider the effect of loading direction. The point of densification (defined further on) in each curve is marked with an open symbol. As expected, the z-axis specimen densifies at a smaller nominal strain. In this direction, band multiplication is confined, at least in the early phases of compression, to the lower density zone where the density is close to that of a y-axis specimen (see Fig. 3). Intuitively, this is

hardly surprising since the thicker cell edges and cell faces in the higher density band have greater bending stiffness and stretch resistances, respectively. This is also reflected in their stress–strain curves: the plateau stresses in both directions agree within the limits of experimental error (they are seen in both the *small* and the *large* cell specimens). The *small* cell foams are nearly twice as stiff and strong compared to the *large* cell ones because size effects affect the latter.

3.1.2. Quasi-static properties

The literature suffers from a lack of consistency in extracting key material parameters (e.g. σ_{cr}^{qs} and ε_D) from a nominal stress–strain curve. The development given below avoids such a problem. The plastic collapse stress σ_{cr}^{qs} (the superscript qs denotes quasi-static loading conditions) is reached when a band of cells start to collapse. This is the first peak stress that separates Phases 2 and 3 in the early deformation response (see Fig. 8b). Its corresponding strain is denoted by ε_{cr}. If the foam is compressed up to a strain of ε_a, the energy absorbed per unit volume is given by (Gibson and Ashby, 1997)

$$W = \int_0^{\varepsilon_a} \sigma_c(\varepsilon)\, d\varepsilon. \tag{11}$$

The efficiency E of the foam in absorbing energy is defined as the energy absorbed up to a given nominal strain, ε_a, divided by the corresponding stress value, i.e.

$$E(\varepsilon_a) = \frac{W}{\sigma_c(\varepsilon)]_{\varepsilon=\varepsilon_a}}, \quad 0 < \varepsilon_a \leqslant 1. \tag{12}$$

A separate study using finite elements (ABAQUS) to model the in-plane compression of honeycombs shows that when opposing walls of their cells crush together, their efficiency reaches a global maximum in the efficiency–strain curve. The details will be published elsewhere (Tan et al., 2005). This idea can be extended, following arguments consistent with Gibson and Ashby (1997), to the more complex geometry of 3D foams so that their densification strain ε_D is also defined by (see Fig. 8c)

$$\left.\frac{dE(\varepsilon)}{d\varepsilon}\right]_{\varepsilon=\varepsilon_D} = 0. \tag{13}$$

There are cases where it is necessary to smooth the efficiency–strain curve before locating its stationary point. Since the densification strain is sensitive to spatial variations of density, only the data obtained from the compression of *y*-axis specimens were fitted to this definition for densification strain giving (the form of the empirical scaling relation was proposed by Ashby et al., 2000)

$$\varepsilon_D = 0.76[1 - 3.17(\rho_o/\rho_s) + 2.17(\rho_o/\rho_s)^3]. \tag{14}$$

To define the plateau stress (especially in the light of its application to dynamic response) the concept of the time average value $\langle f \rangle$ of a smooth and continuous function $f(t)$ is utilised. The strain axis of the stress–strain curve is converted into

time by using

$$t = \varepsilon \cdot l_{\mathrm{o}}/\dot{\delta}, \tag{15}$$

where the quasi-static compression rate $\dot{\delta} = 45\,\mu\mathrm{m\,s^{-1}}$. The plateau stress $\sigma_{\mathrm{pl}}^{\mathrm{qs}}$ is defined as the time average value of the function $\sigma_{\mathrm{c}}(t)$ so, as illustrated in Fig. 9, the rectangular area $(t_{\mathrm{D}} - t_{\mathrm{cr}})\langle\sigma_{\mathrm{c}}\rangle$ is equal to the actual area under the curve in the interval $t_{\mathrm{cr}} \leqslant t \leqslant t_{\mathrm{D}}$ as follows:

$$\sigma_{\mathrm{pl}}^{\mathrm{qs}} = \langle\sigma_{\mathrm{c}}\rangle \equiv \frac{1}{(t_{\mathrm{D}} - t_{\mathrm{cr}})} \int_{t_{\mathrm{cr}}}^{t_{\mathrm{D}}} \sigma_{\mathrm{c}}(t)\,\mathrm{d}t, \tag{16}$$

where t_{cr} and t_{D} is related to $\varepsilon_{\mathrm{cr}}$ and ε_{D}, respectively, through Eq. (15). If plastic collapse of the foam results in a perfectly plastic stress–strain response then Eq. (16) gives $\sigma_{\mathrm{pl}}^{\mathrm{qs}} = \sigma_{\mathrm{cr}}^{\mathrm{qs}}$, as expected.

The theoretical plastic collapse strength of closed-cell foams (the contribution of gas pressure is discussed later) is (Gibson and Ashby, 1997)

$$\sigma_{\mathrm{cr}}^{\mathrm{qs}}/\sigma_{\mathrm{ys}} \approx 0.3(\phi\rho_{\mathrm{o}}/\rho_{\mathrm{s}})^{3/2} + (1 - \phi)\rho_{\mathrm{o}}/\rho_{\mathrm{s}}, \tag{17}$$

where ϕ is the fraction of solid in the cell edges; the remaining fraction $(1 - \phi)$ of solid is contained in the cell faces. Experimental data for the plastic collapse strength of the foam specimens and the predictions by Eq. (17) (for different values of ϕ) are plotted in Fig. 10. The large scatter in the data reflects the sensitivity of the plastic collapse stress to local heterogeneities, such as density variations and cell morphological defects, within the collapsing band of cells. All the data lie close to $\phi \approx 1$: this suggests that they deform primarily through cell edge bending—in essence they behave like open cell foams. Two reasons for this are that the cell faces may have ruptured before plastic collapse and the contribution of the cell faces, though still present, is comparatively small and negligible (Gibson and Ashby, 1997). The data for the *large* cell specimens lies beyond the limiting value of $\phi = 1$. This is because they are affected by cell-size effects, since $d_{\mathrm{o}}/\bar{d} < 5$ for the *large* cell specimens, which occur in specimens where the reduced constraint of the cell walls at the free surface is coupled with an increased area fraction of stress-free
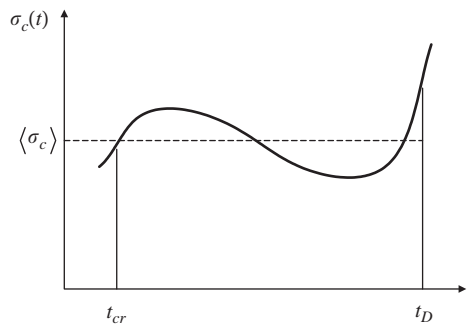

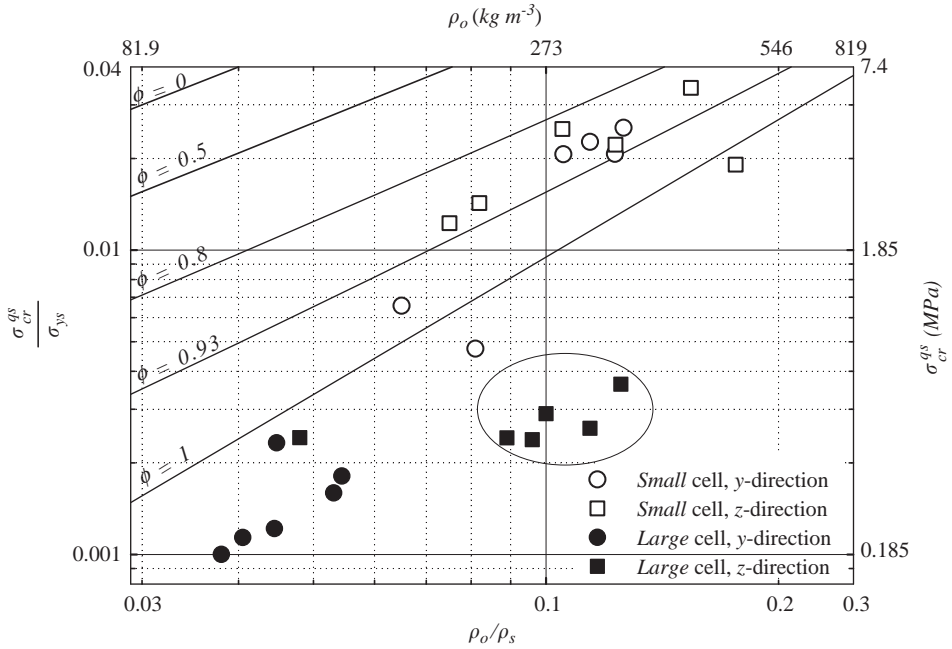Fig. 9. The definition of plateau stress for the function $\sigma_{\mathrm{c}}(t)$.

Fig. 10. Data for the plastic collapse stress $\sigma_{cr}^{qs}/\sigma_{ys}$ plotted against relative density ρ_o/ρ_s. The bubble indicates the region of super-imposed density dependence between the *small* and the *large* cell specimens.

cell walls (Andrews et al., 2001). Due to reasons stated above, the data for the *large* cell specimens, unlike its *small* cell counterpart, cannot be treated as representative of the Hydro/Cymat foam properties. Rather, their inclusion is used here to elucidate how cell-size affects the static and dynamic strength properties.

The scaling relation in Eq. (17) requires a unique and single-valued correspondence between the domain of definition (relative density) and the strength property. As pointed out earlier, the *z*-axis specimens have strength properties that are lower than what their relative density would, normally, predict. This is particularly evident for the *large* cell specimens (the anomaly is enclosed within the bubble-region in Fig. 10). Because of the super-imposed density dependence, separate characteristic curves were used to fit the data for the different average cell sizes. Although the response of the foam is not perfectly plastic, the same scaling law was used to fit the data for the plateau strength also. As shown in Fig. 10, the dependence of all the strength data on ρ_o/ρ_s are adequately described by Eq. (17) with $\phi = 1$ and there appears to be little evidence of the influence of membrane stress. The scatter in strength properties for the *small* and *large* cell specimens with similar relative densities is in the order of $\pm 20\%$ and $\pm 40\%$, respectively.

By setting $\phi = 1$, the experimental data is fitted to the scaling relation in Eq. (17) to give (see Fig. 11)
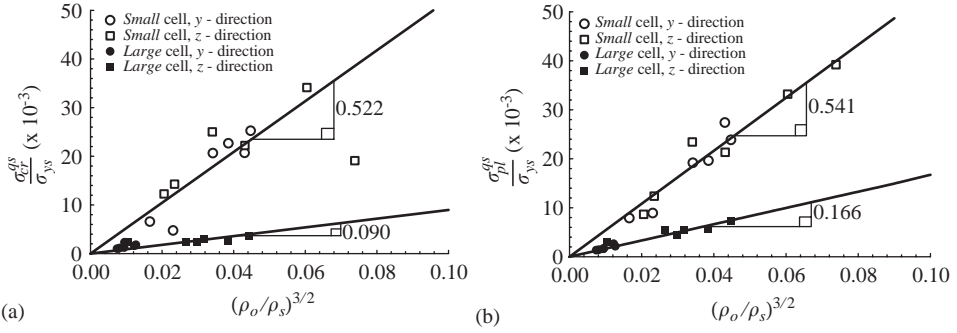
Fig. 11. Data for the quasi-static (a) plastic collapse and (b) plateau stresses (normalised by the yield strength of the cell wall material) plotted against relative density $(\rho_o/\rho_s)^{1.5}$. The solid lines represent the scaling relation given by Eq. (17) with $\phi = 1$.

For small cell foams:

$$\sigma_{cr}^{qs}/\sigma_{ys} = C_1(\rho_o/\rho_s)^{3/2} = 0.522(\rho_o/\rho_s)^{3/2}, \tag{18}$$

$$\sigma_{pl}^{qs}/\sigma_{ys} = C_2(\rho_o/\rho_s)^{3/2} = 0.541(\rho_o/\rho_s)^{3/2}. \tag{19}$$

For large cell foams:

$$\sigma_{cr}^{qs}/\sigma_{ys} = C_3(\rho_o/\rho_s)^{3/2} = 0.090(\rho_o/\rho_s)^{3/2}, \tag{20}$$

$$\sigma_{pl}^{qs}/\sigma_{ys} = C_4(\rho_o/\rho_s)^{3/2} = 0.166(\rho_o/\rho_s)^{3/2}. \tag{21}$$

3.1.3. Effect of gas contributions to the strength properties

When closed-cell foam undergoes plastic collapse the fluid in the cells is compressed too. Hence, the gas pressure contribution must be added to Eq. (17). A first-order estimate of this can be made by assuming that the ideal gas in the cells undergoes isothermal compression to give a strength elevation of (Gibson and Ashby, 1997)

$$\Delta\sigma = \frac{P_o \varepsilon_D (1 - 2v_f)}{[1 - \varepsilon_D(1 - 2v_f) - \rho_o/\rho_s]}, \tag{22}$$

where P_o (= 0.1 MPa) is the atmospheric pressure. A similar calculation, assuming adiabatic compression, gives (Gibson and Ashby, 1997)

$$\Delta\sigma = P_o\left[\left(\frac{1 - \rho_o/\rho_s}{1 - \varepsilon_D(1 - 2v_f) - \rho_o/\rho_s}\right)^\gamma - 1\right], \tag{23}$$

where γ (= 1.4 for air) is the ratio of specific heat capacities. For a typical *small* cell specimen ($\rho_o = 350\,\mathrm{kg\,m^{-3}}$, $v_f \approx 0.32$, $\varepsilon_D = 0.445$), the predicted strength elevation by Eqs. (22) and (23) is approximately 0.02 and 0.03 MPa, respectively. Similarly, gas pressure contribution in a typical *large* cell specimen ($\rho_o = 135\,\mathrm{kg\,m^{-3}}$, $v_f \approx 0.32$, $\varepsilon_D = 0.641$) is approximately 0.03 and 0.05 MPa, respectively. In each case, the

strength elevations are less than their respective limits of experimental error; therefore, following Deshpande and Fleck (2000), it is concluded that the contribution of gas pressure to the measured strength properties is so small as to be negligible.

3.2. Dynamic compression

As noted in Sections 1 and 2, 45 mm diameter specimens were compressed dynamically under uniaxial strain conditions at impact velocities of up to $210\,\mathrm{ms}^{-1}$. Under impact loading their cells, too, deform by cell edge bending and cell face stretching. However, the inertia of the cell walls modifies the local quasi-static collapse mechanism, leading to less compliant modes, which require higher loads to cause cell crushing. The response to dynamic loading in the y-direction is presented first. In this direction, the density distribution in the specimen is relatively uniform.

3.2.1. Loading in the y-direction
3.2.1.1. Force pulses.
Typical force pulses measured at different impact velocities are shown in Fig. 12. Their time and nominal strain axes are linearly related if the specimens are compressed at a uniform rate. However, this can only be achieved with a high mass ratio, say $M_r > 100$. If the duration of the force pulse (total time required for the specimen to fully crush) is greater than the bar transit time then the pulse is affected by wave reflection from the free end of the bar, as in Figs. 12a, b and d.
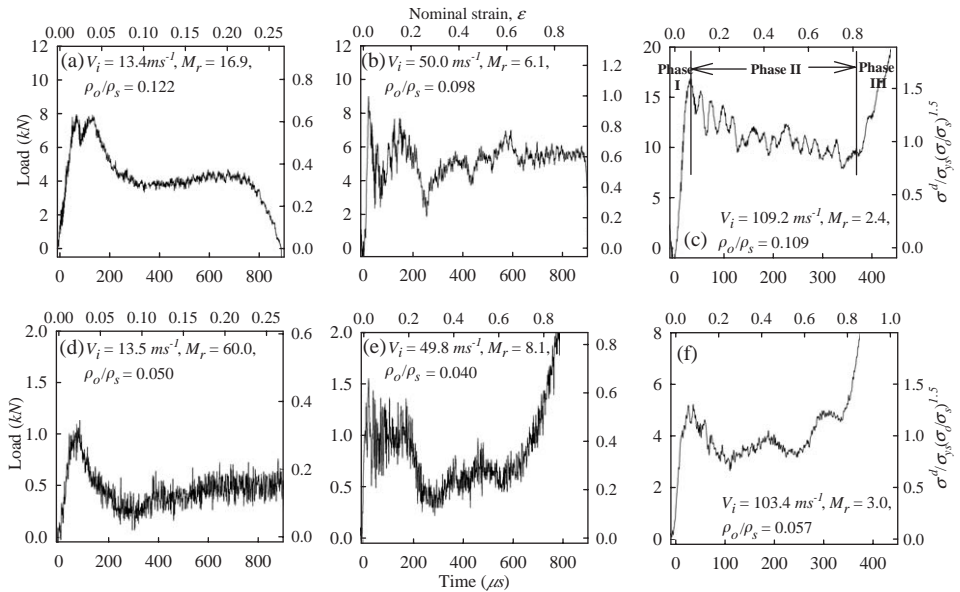

Fig. 12. Typical dynamic force pulses for *small* (a–c) and *large* (d–f) cell cylindrical y-axis specimens measured by direct impact.

Similar to Fig. 8, deformation of the specimen occurred in three phases: an initial phase leading to peak deceleration (I); a crushing phase (II); and, a densification phase (III)—see Fig. 12c. Phase I deformation corresponds to the initiation of elastic cell deformation by this wave. At a cell level, the disturbance propagates as flexural waves in the cell edges and faces.

Phase II deformation begins when plastic collapse first occurs in a band of cells at the weakest section of the specimen and this is accompanied by a drop in the load. Fig. 13 shows two contrasting distributions of cell deformation in *small* cell specimens: one partially crushed at a sub-critical velocity (see definition below) of $22.4\,\text{ms}^{-1}$ (Fig. 13b), and the other at a super-critical velocity of $107.5\,\text{ms}^{-1}$ (Fig. 13a). Both had insufficient energy to achieve full crushing. The latter had no backing mass ($M_r = 0$), similar to a Taylor bullet test. The continuous transit of an elastic wave in the rear portion of the specimen reflected between the crush front and the rear (distal) stress-free end eventually brings the specimen to rest after many traversals in the rear part of the specimen. There were, however, important differences in the development and the distribution of cell deformation between the two specimens that depended to a large extent on the impact velocity. A critical velocity corresponding to a transition in the location and nature of the deformation is estimated later.

At a sub-critical velocity (Fig. 13b) the deformation pattern is similar to quasi-static loading, the plastic collapse initiating at the weakest band of cells, almost always in the interior of the specimen. The layer of cells at the impact surface is reinforced by their contact with the anvil and this makes geometric softening in them much more difficult (Papka and Kyriakides, 1994). For this reason, plastic collapse of the cells at the impact surface usually occurs in the latter stages of Phase II deformation. There are, however, exceptions depending on the distribution, the severity and the types of cell defects present. Overall shortening of the specimen is by the accumulation of discrete, non-contiguous bands of crushed cells as in quasi-static compression.

At a super-critical velocity (Fig. 13a), the impulse generated by impact is so severe that the cells at the impact surface undergo rapid plastic collapse and densify. The residual momentum is then transferred to an adjacent layer of cells, in a 'domino-type' effect, so that cell crushing (or compaction) occurs sequentially, in a planar manner, along the axis of the specimen from the impact-end. This is irrespective of whether the cell deformation mechanism is stable or unstable. With reference to the initial un-deformed configuration of the specimen, a planar cross-sectional surface, separating the crushed and the uncrushed cells, of approximately one cell-width (hereinafter, called the crush front), can be seen to propagate along the axis of the specimen with time. Such a phenomenon is clearly evident in the high-speed photographic sequence by Radford et al. (2005), and in finite-element simulations of 2D cellular structures (see Part II). Because unloading from partially compacted states involves only a small volume recovery, the interface remains visible in the fully unloaded specimen shown in Fig. 13a. Since the particle velocity and the deformation gradient (strain) in the specimen suffer rapid, finite changes across a propagating, narrow surface, it called a 'shock' wave here, idealised as a first-order
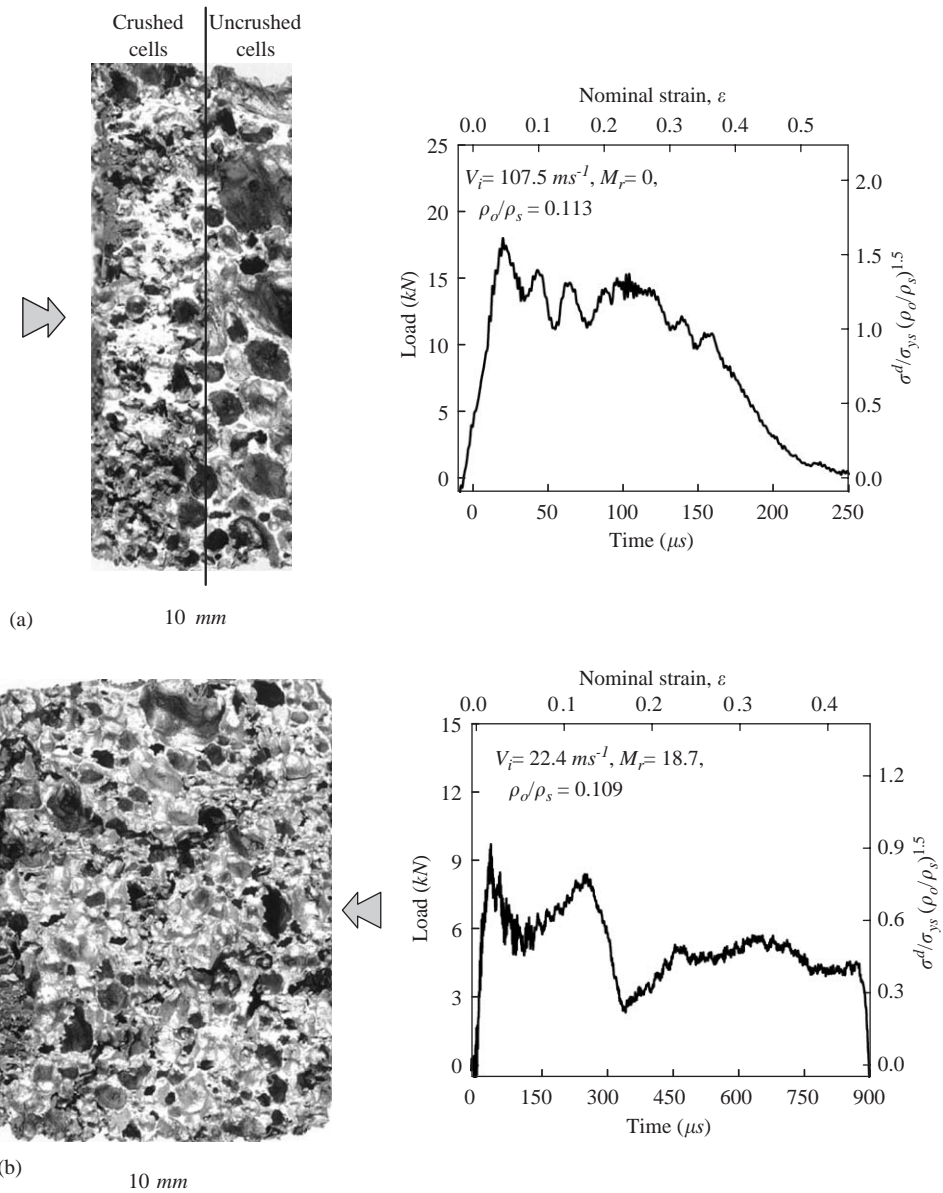
Fig. 13. Typical distributions of cell deformation and their corresponding force pulse for two *small*-cell, *y*-axis specimens crushed at (a) super-critical and (b) sub-critical velocities. A planar cross-sectional surface separates the crushed and uncrushed cells in (a) whilst the discrete bands of crushed cells are visible in (b). The arrowhead denotes the impact end.

singular surface (Eringen and şuhubi, 1974). A 'shock' was considered to form immediately in the foam specimen, across which the basic jump conditions were assumed to hold. The typical force pulse measured exhibited successive decreasing

peaks with time (an example of the force pulse for a fully crushed specimen at a super-critical velocity is shown in Fig. 12c): this is similar to that obtained from simulations using a heuristic spring–mass model by Shim et al. (1990). The decreasing peak forces are due to the decreasing momentum flux at the crushing wave front with time. If all the cells in the specimen have collapsed and the energy of impact is not yet completely dissipated, compression of the cell wall material will occur if $M_r > 0$ and this is reflected in the rapidly stiffening régime of Phase III (Fig. 12c). Otherwise, Phase III will be absent from the force pulse measured (Fig. 13a). It is interesting to note that similar 'shock'-type deformation response is also observed in the high-velocity crushing of wood, of cellular structures (Reid et al., 1993; Reid and Peng, 1997), and of honeycombs (Reid et al., 1993; Ruan et al., 2003).

3.2.1.2. Strength properties.   The procedure to extract the key material parameters from a dynamic force pulse paralleled that for the quasi-static nominal stress–strain curve closely and is not repeated here. For the same reason given in Section 3.1.2, only the data for the *small* cell specimen are representative of the Hydro/Cymat foam properties. Those of the *large* cell specimen are used to explain how size effects could affect their dynamic strength.

Data for the plastic collapse stress, σ_{cr}^d, of *small* and *large* cell foams at different impact velocities are plotted in Fig. 14. They are normalised by $(\rho_o/\rho_s)^{3/2}$ to account for the different densities of the specimens (Ashby et al., 2000). The stress ratio Π ($\equiv \sigma_{cr}^d/\sigma_{cr}^{qs}$) is defined as the ratio of the dynamic to the quasi-static plastic collapse stress. Using the criterion proposed by Deshpande and Fleck (2000), the dynamic stress is said to be enhanced if, and only if, it exceeds the upper strength limit of the quasi-static scatter, i.e. $\sigma_{cr}^d > 1.2\sigma_{cr}^{qs}$ (for *small* cell foam) and $\sigma_{cr}^d > 1.4\sigma_{cr}^{qs}$ (for *large* cell foam). The data shows significant crushing strength enhancement for both the *small* and *large* cell specimens over the entire range of velocity. This is in spite of using the raw data for the latter.

Based on the calculations in Section 3.1.3, the contribution to the Phase I enhancement from the compression of the trapped gas is estimated to be small enough to be negligible. Deshpande and Fleck (2000) found that the strain rate in the cell edges in open cell foam is approximately an order of magnitude lower than its nominal compression rate $\dot{\varepsilon}$. Since this was less than $5000\,s^{-1}$ in all our tests, it is concluded here that the material strain rate sensitivity of the aluminium-based cell wall is also negligible. The main contention herein is that inertial/velocity sensitivity is the most dominant effect in the tests reported. This results in a delay in triggering a buckling collapse mode and/or from the generation of an alternative less complaint cell collapse mechanism than that occurring in quasi-static compression (Reid et al., 1993). The effect is analogous to the lateral inertia forces that developed in the arms of a typical Type II strut. These have the effect of introducing an initial phase of deformation where axial plastic axial compression of the strut dominates (Calladine and English, 1984; Su et al., 1995; Karagiozova and Jones, 1995). In this phase a considerable portion of the kinetic energy of the mass is absorbed before a bending mechanism predominates leading to an enhancement of the plastic collapse load.
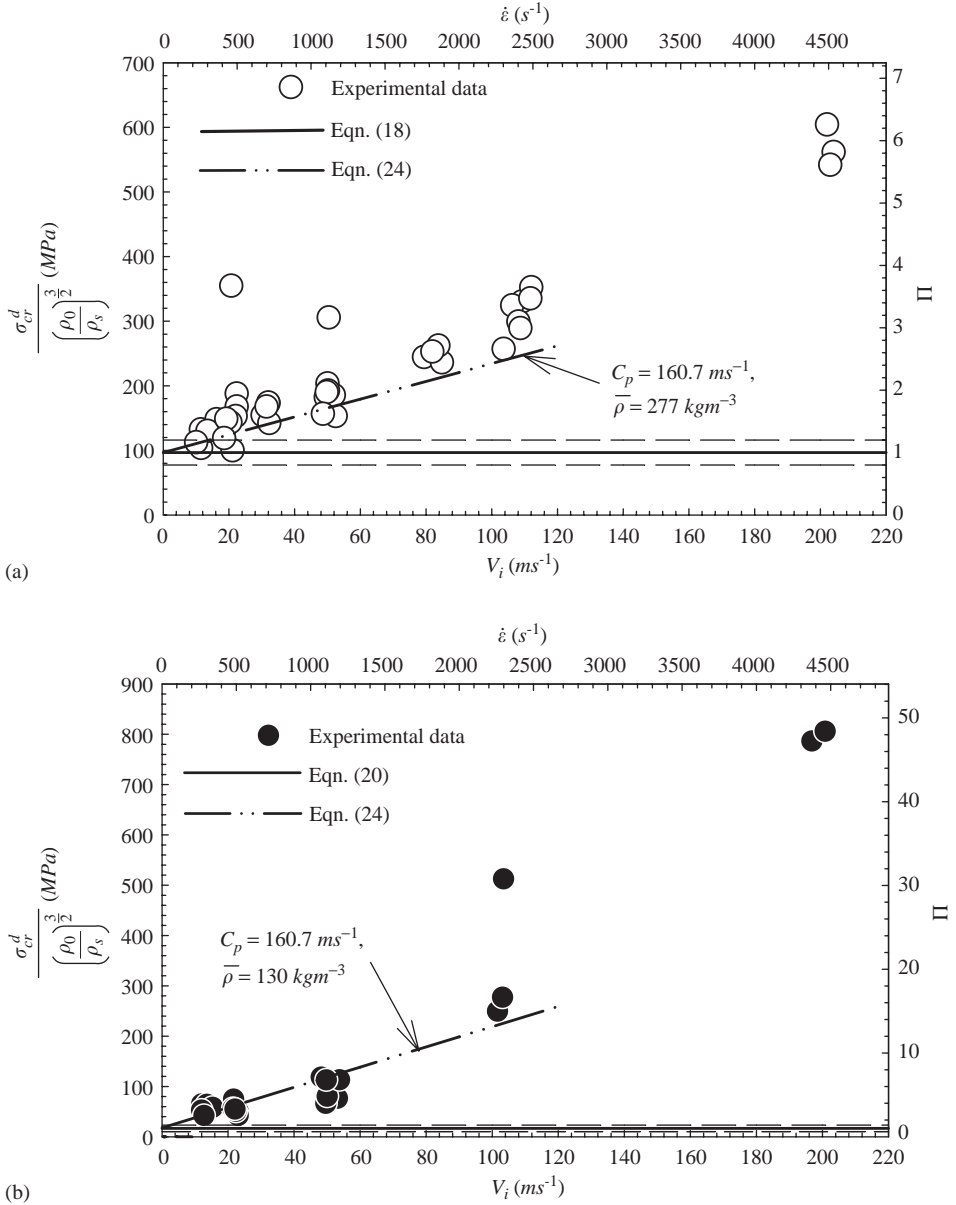
Fig. 14. Variation of the normalised plastic collapse stress $\sigma_{cr}^d/(\rho_o/\rho_s)^{1.5}$ th impact velocity V_i for (a) *small* cell and (b) *large* cell y-axis specimens. The dashed lines indicate corresponding quasi-static scatter in loads and $\dot{\varepsilon}$ is the nominal engineering strain rate.

Studies on the dynamic in-plane compression of honeycombs (Klintworth, 1988; Hönig and Stronge, 2002) have established that the rotational and translational inertia of the cell edges are both responsible for this effect. The same explanation can

be extended qualitatively to the 3D cell geometries of the foam specimens. Numerical models of 2D honeycombs and Voronoi structures (see Hönig and Stronge (2002) and Part II) reveal such effects. The experimental data also support this contention.

The data for σ_{cr}^d in Fig. 14 approximately vary linearly with impact velocity, in particular at the lower velocities. This is consistent with the stress level being controlled by axial plastic wave propagation in the cell walls. If the aluminium cell wall material has a 'bi-linear' stress–strain relation, this wave travels at the plastic wave speed C_p ($\equiv \sqrt{E_p/\rho_s}$, where E_p is the plastic modulus). Since $E_p \approx 70.5$ MPa for aluminium, the plastic wave speed is given by $C_p \approx 160.7$ ms^{-1}. Hence, the dynamic plastic collapse stress will vary linearly with the impact velocity according to

$$\sigma_{cr}^d = \sigma_{cr}^{qs} + \bar{\rho} C_p V_i, \tag{24}$$

where $\bar{\rho} = \sum_N (\rho_o)_N / N$ is the average density of specimens tested. Eq. (24) fits the data reasonably well, at the lower velocities, in Fig. 14. Calladine and English (1984) correctly described this as a 'velocity' rather than a (nominal) strain-rate effect.

The plateau stress in Phase II, a time averaged value of the force pulse divided by A_o, is associated with the multiplication of discrete bands of crushed cells. Data for the normalised plateau stress $(\sigma_{pl}^d / \rho_o / \rho_s)^{3/2})$ and the stress ratio ($\Pi \equiv \sigma_{pl}^d / \sigma_{pl}^{qs}$) of *small* and *large* cell foams obtained at different impact velocities are plotted in Fig. 15. They exhibit an approximately quadratic dependence on the impact velocity. The difference between the plastic collapse and the plateau stress of each specimen increases with impact velocity (compare Figs. 14 and 15), the former being the higher of the two values. At the lower impact velocities the plateau stress is often smaller than its corresponding quasi-static value probably because of the effect of internal elastic wave reflections. If the dynamic plateau stress is said to be enhanced only when it exceeds the upper strength limit of their quasi-static scatter (Deshpande and Fleck, 2000), then Fig. 15 shows that the dynamic plateau stresses are insensitive to impact velocity below the values of ~50 and ~80 ms^{-1} for the *large* and *small* cell specimens, respectively.

As noted in Section 3.2.1(i) above, a switch in the deformation pattern, from a discrete crush band multiplication in Fig. 13b to a progressive cell crushing in Fig. 13a, occurs when the impact velocity exceeds a critical value. It is contended here that sequential cell crushing occurs when the kinetic energy of a band of collapsing cells crosses a critical energy barrier. It will be shown in Part II using thermodynamics arguments that, for a r-p-p-l material, this occurs at an impact velocity of approximately

$$V_{cr} = (2 C_n \sigma_{ys} / \rho_s)^{1/2} (\rho_o / \rho_s)^{1/4} \varepsilon_D^{1/2}, \tag{25}$$

where the subscript $n = 1$ (*small* cell) or 3 (*large* cell). The predicted critical velocity is 107.9 and 41.5 ms^{-1} for the *small* (using $\rho_o / \rho_s = 0.101$) and *large* (using $\rho_o / \rho_s = 0.048$) cell foam, respectively. This agrees with the data plotted in Fig. 14. At sub-critical velocities, i.e. approximately $V_i < 108$ ms^{-1}, the normalised plastic collapse stress of *small* cell specimens is greater than their corresponding *large* cell ones. This suggests that specimen cell-size effects and strength degradation due to morphological imperfections remains active. At super-critical velocities of
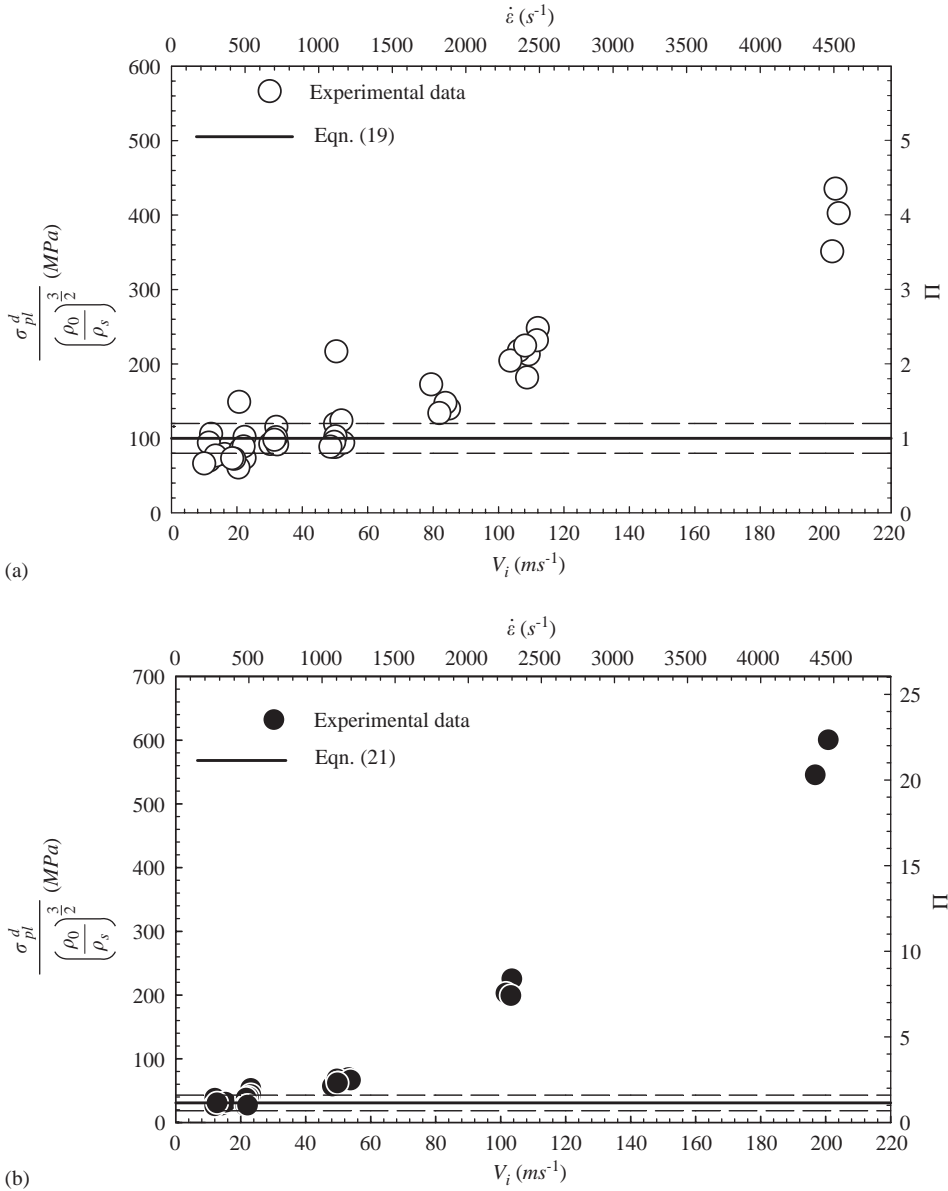
Fig. 15. Variation of the normalised plateau stress $\sigma_{pl}^{d}/(\rho_o/\rho_s)^{1.5}$ with impact velocity V_i for (a) *small* cell and (b) *large* cell y-axis specimens. The dashed lines indicate corresponding quasi-static scatter in loads and $\dot{\varepsilon}$ is the nominal engineering strain rate.

$V_i > 108\,\mathrm{ms}^{-1}$, the strength data are no longer affected by these, the strength for the *large* cell specimens being greater than the *small* cell specimens at each velocity. This implies, in particular, that further local enhancements in strength are now dominated

by a different inertial phenomenon associated with the dynamic localisation of crushing, i.e. the deformation response begins to exhibit 'shock-like' characteristics (Reid and Peng, 1997).

If the time axis of the force pulses in Figs. 12a–c is converted into displacement of the distal end to produce nominal stress–strain curves (assuming a uniform rate of compression so that $\delta = V_i \cdot t$), the greater amount of energy (normalised by $(\rho_o/\rho_s)^{3/2}$) absorbed at higher impact velocities with similar displacements is clearly evident in the approximate energy versus displacement plots in Fig. 16. The theoretical explanation for this will be given in Part II.

3.2.2. Loading in the z-direction

Since the z-axis specimens have spatial variations (step-distributions) of density, tests were carried out to measure the impact forces generated by impact on either the high-(HD) or the low-(LD) density end of each specimen. Fig. 17 shows two partially crushed *small* cell specimens (compressed at a velocity of approximately $23\,\mathrm{ms}^{-1}$) and their corresponding normalised stress pulses. The specimen with a higher mass ratio is compressed further by virtue of its higher kinetic energy. An unusually high level for the plastic collapse stress was recorded if the HD end of the specimen impacts the output bar (Fig. 17a). This was seen in both the *small* and *large* cell specimens over the entire range of velocity. It suggests that cell deformation may have occurred in the HD zone of the specimen where a higher load is needed to overcome the inertia of the thicker cell walls. Its photograph shows limited cell crushing, not readily discernible by observation, in the HD zone. If impact occurs at the LD end of the specimen, the HD zone behaves like a rigid material so that cell crushing is confined, at least during the early period of Phase II, to the LD zone (Fig. 17b). Fig. 17 shows that Phase II deformation is dominated by the multiplication of bands of crushed cells in the LD zone, regardless of which end of the specimen strikes the transmitter bar (see photographs). This is also reflected in their plateau strength, which agrees with one another within the limits of
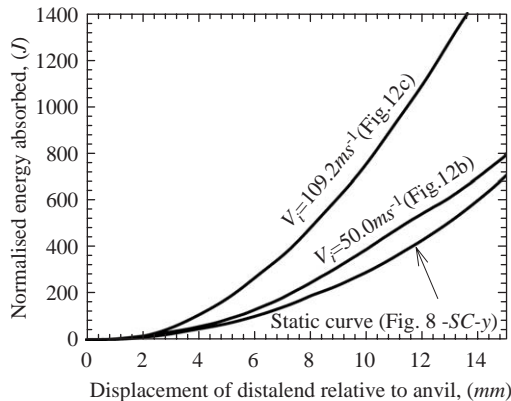

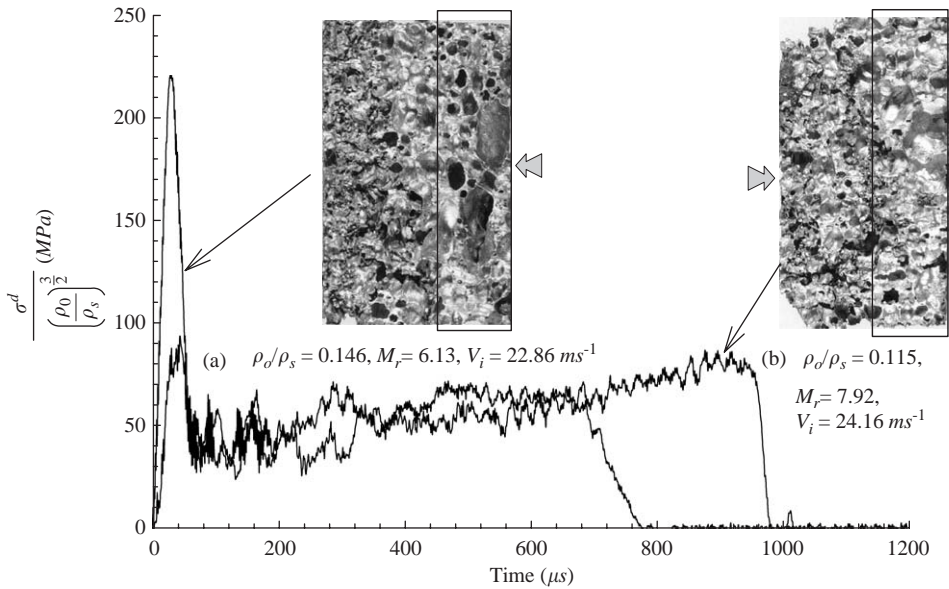Fig. 16. Static and dynamic normalised energy versus displacement curves.

Fig. 17. Two *small* cell, *z*-axis specimens and their corresponding normalised stress pulses measured from the (a) HD and the (b) LD end of each specimen. The arrowhead indicates the impact end and the HD zone of each specimen are boxed.

experimental error. In general, the dynamic strength properties, the initiation, development and distribution of cell deformation and the densification strain of a specimen are all affected by spatial variations of density. Their implications must be considered when, for example, a foam panel is used for impact energy absorption purposes.

3.2.3. Effects of specimen length

To investigate the effects of specimen gauge length, tests (quasi-static and dynamic) were carried out using only *small* cell, *y*-axis specimens, of 45 mm diameter, with gauge lengths ranging from $5\,\text{mm} \leqslant l_o \leqslant 65\,\text{mm}$. Hence, they were not affected by the size effect described in Section 3.1.2. The smallest gauge length used was 5 mm because of difficulties with machining shorter specimens. Test specimens of different gauge length were first compressed at a constant velocity (the largest backing mass that will not yield the pressure bar was used). This was then repeated for different impact velocities (up to $100\,\text{ms}^{-1}$) to build up a family of curves. The objective was to separate the rate sensitive response due to an increase in the impact velocity (V_i) from the length effects caused by changes in the gauge length (l_o) of the specimen. Note that the latter is another type of 'size' effect different from the one discussed in Section 3.1.2.

Data for the normalised plateau stress ($\sigma_{pl}/[\sigma_{ys}(\rho_o/\rho_s)^{1.5}]$) of specimens with different gauge length are plotted in Fig. 18. The solid lines are predictions produced
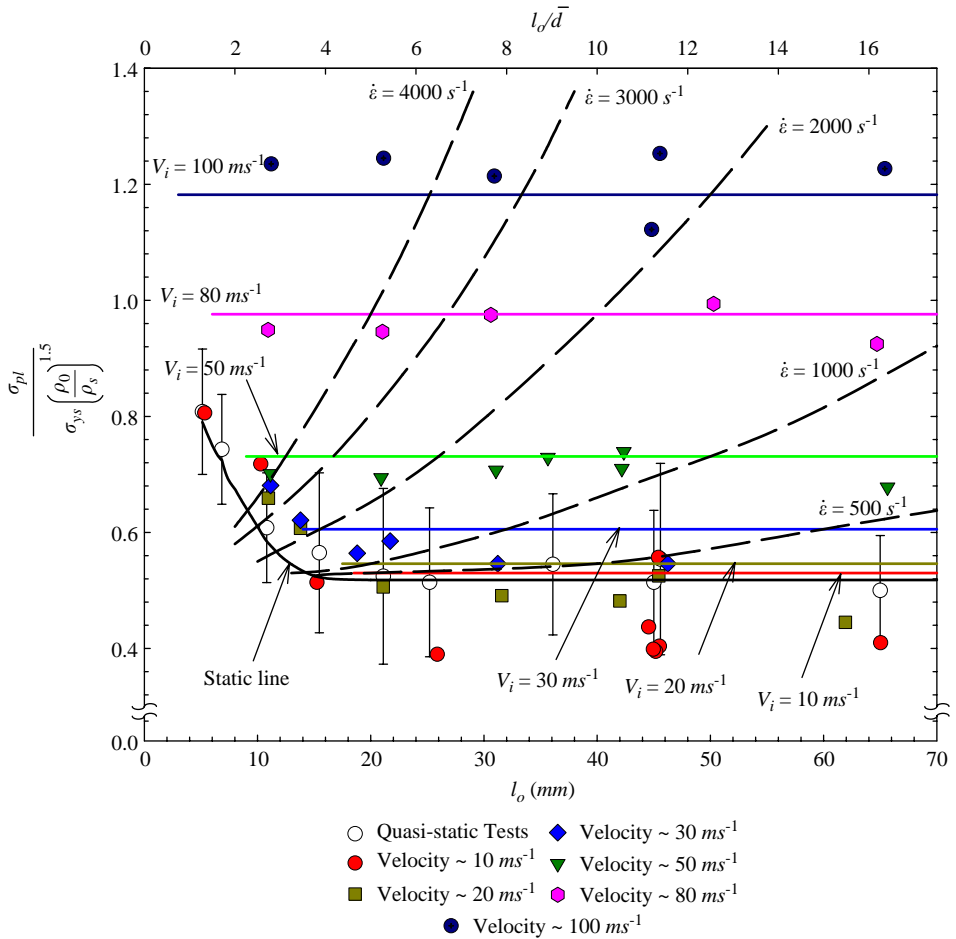
Fig. 18. Normalised plateau stresses of *small* cell, *y*-axis specimens with different gauge length and impact velocity. Solids lines are predictions by Eq. (26) (dynamic test) and Eq. (19) (quasi-static test). Dashed lines are family of constant nominal engineering strain rates.

by a 1D 'shock' model (Reid and Peng, 1997):

$$\sigma_{pl}^{d} = \sigma_{pl}^{qs} + \bar{\rho} V_i^2 / \varepsilon_D, \tag{26}$$

where $\bar{\rho}$ is the average density of the specimens tested at each velocity. The dashed lines are curves of constant nominal, engineering strain rate. The resulting diagram allows some important features of specimen length scale to be illustrated. First, the shorter specimens have a stronger and stiffer response under quasi-static compression. Mukai et al. (1999) also reported a similar observation with closed cell Alporas foams. This length effect persists to a value of approximately 5 average cell diameter, beyond which fluctuations in the strength property are within ±20% of

its mean value predicted by Eq. (18). This unusual response is probably due to end-effects in the shorter specimens where geometric softening in the two end rows of cells is made more difficult, or suppressed entirely, through its contact with the rigid platen. The data presented agree with the surface deformation analysis by Bastawros et al. (2000) who also reported that the localised bands in Alporas foam exhibit a 'long-range' correlation of approximately 3–5 cells. Second, a similar length effect is also detected in specimens under dynamic loading. Their plastic collapse stresses decrease with increasing gauge length, but at increasingly higher stresses as the impact velocity was increased. The number of cells to which this length effect persists reduces from ∼5 at $10 \, \mathrm{ms^{-1}}$ to ∼2 cells at $80 \, \mathrm{ms^{-1}}$. However the effects of specimen gauge length became less significant, compared to the velocity sensitive response of the foams, at increasingly higher velocities. Fig. 18 shows that there is a characteristic length associated with an accommodation domain which sets a limit to the minimum material volume required for a valid continuum approximation. The minimum gauge length required to achieve the bulk strength of Cymat/Hydro foams is, at least, 5 average cell diameters. Lastly, the figure shows that *there is no correlation between the dynamic strength properties and the nominal engineering strain rate*. The velocity dependence of the strength properties and the irrelevance of nominal engineering strain rate are clearly illustrated in Fig. 18. This is the one of the main reasons for the conflicting conclusions on the correlation between loading rate and dynamic strength of foams to be found in the literature.

4. Conclusion

The strength properties of Cymat/Hydro foam have been measured and their response to dynamic loadings has been described. A consistent framework has been proposed to extract key material parameters (the plastic collapse and the plateau stress, and the strain at which densification occurs) from nominal stress–strain curves and dynamic force pulses. Their dynamic response depended on the direction of loading relative to the cell geometry (y or z) and on the loading velocity.

The density gradient in z-axis specimens is responsible for the unusually high plastic collapse load measured under impact loading conditions.

It was estimated that the transition to a 'shock-type' deformation response occurs at an impact velocity of approximately 108 and $42 \, \mathrm{ms^{-1}}$ for *small* and *large* cell foam, respectively. This compares well with the experimental data. Inertia effects associated with the dynamic localisation of crushing are responsible for the enhancement of the dynamic strength properties measured at super-critical impact velocities where specimen size effects and cell morphological defects are insignificant. In the sub-critical velocity régime, both the specimen cell-size effects and cell morphological defects affect the dynamic strength properties measured. Micro-inertial effects are responsible for the enhancement of the dynamic plastic collapse stress at the sub-critical velocities. Post-impact examination of partially crushed specimens showed that deformation is through the cumulative multiplication of discrete crush bands for static loading and for dynamic loading at sub-critical impact

velocities. At super-critical impact velocities, specimens deform by progressive cell crushing from the impact surface.

Acknowledgements

References

Andrews, E.W., Gioux, G., Onck, P., Gibson, L.J., 2001. Size effects in ductile cellular solids, Part II: experimental results. Int. J. Mech. Sci. 43, 701–713.

Arfken, G.B., Weber, H.J., 1995. Mathematical for Methods Physicist, fourth ed. Academic Press, California.

Ashby, M.F., Evans, A.G., Fleck, N.A., Gibson, L.J., Hutchinson, J.W., Wadley, H.N.G., 2000. Metal Foams: A Design Guide. Butterworth Heinemann, Oxford.

Bacon, C., 1998. An experimental method for considering dispersion and attenuation in a viscoelastic Hopkinson bar. Exp. Mech. 38, 242–249.

Bacon, C., 1999. Separation of waves propagating in an elastic or viscoelastic Hopkinson pressure bar with three-dimensional effects. Int. J. Impact Eng. 22, 55–69.

Bastawros, A.F., Bart-Smith, H., Evans, A.G., 2000. Experimental analysis of deformation mechanisms in a closed-cell aluminum alloy foam. J. Mech. Phys. Solids 48, 301–322.

Brillouin, L., 1946. Wave Motion in Periodic Structures. McGraw-Hill, New York.

Calladine, C.R., English, R.W., 1984. Strain-rate and inertia effects in the collapse of two types of energy-absorbing structure. Int. J. Mech. Sci. 26, 689–701.

Chastel, Y., Hudry, E., Forest, S., Peytour, C., 1999. Mechanical behaviour of aluminium foams for various deformation paths: experiment and modelling. In: Banhart, J., Ashby, M.F., Fleck, N.A. (Eds.), Cellular Metals and Metal Foaming Technology. Verlag MIT Publishing, Bremen, Germany, pp. 263–268.

Chen, C., Lu, T.J., Fleck, N.A., 1999. Effect of imperfections on the yielding of two dimensional foams. J. Mech. Phys. Solids 47, 2235–2272.

Davies, E.D.H., Hunter, S.C., 1963. The dynamic compression testing of solids by the method of the split Hopkinson pressure bar (SHPB). J. Mech. Phys. Solids 11, 155–179.

Deshpande, V.S., Fleck, N.A., 2000. High strain rate compressive behaviour of aluminium alloy foams. Int. J. Impact Eng. 24, 277–298.

Eringen, A.C., Şuhubi, E.S., 1974. Elastodynamics, vol. 1–Finite Motions. Academic Press, New York.

Gibson, L.J., Ashby, M.F., 1997. Cellular Solids: Structure and Properties, second ed. Cambridge University Press, Cambridge.

Gorham, D.A., Pope, P.H., Field, J.E., 1992. An improved method for compressive stress–strain measurements at very high strain rates. Proc. R. Soc. London A 438, 153–170.

Hanssen, A.G., 2000. Private Communication.

Harrigan, J.J., Reid, S.R., Reddy, T.Y., 1998a. Inertial forces on the crushing of wood loaded along the grain. In: Allison, I.M. (Ed.), Experimental Mechanics. Balkema, Rotterdam, pp. 193–198.

Harrigan, J.J., Reid, S.R., Reddy, T.Y., 1998b. Accurate measurement of impact force pulses in deforming structural components. In: Allison, I.M. (Ed.), Experimental Mechanics. Balkema, Rotterdam, pp. 149–154.

Harte, A.M., Nichol, S., 2001. Scale-up issues related to producing Cymat stabilised aluminium foam. In: Banhart, J., Ashby, M.F., Fleck, N.A. (Eds.), Cellular Metals and Metal Foaming Technology. Verlag MIT Publishing, Bremen, Germany, pp. 49–54.

Hönig, A., Stronge, W.J., 2002. In-plane dynamic crushing of honeycomb—Part I: crush band initiation and wave trapping. Int. J. Mech. Sci. 44, 1665–1696.

Inoue, H., Kamibayashi, M., Kishimoto, K., Shibuya, T., Koizumi, T., 1992. Numerical Laplace transformation and inversion using fast Fourier transformation. JSME Int. J. 35, 319–324.

Inoue, H., Harrigan, J.J., Reid, S.R., 2001. A review on inverse analysis for indirect measurement of impact force. ASME Appl. Mech. Rev. 54, 503–524.

Karagiozova, D., Jones, N., 1995. A note on the inertia and strain-rate effects in the Tam and Calladine model. Int. J. Impact Eng. 16, 637–649.

Kenny, L.D., 1996. Mechanical properties of particle stabilised aluminium foam. Mater. Sci. Forum 217-222, 1883–1890.

Klintworth, J.W., 1988. Dynamic crushing of cellular solids. Ph.D. Thesis, University of Cambridge.

Lankford, J., Danneman, K.A., 1998. Strain rate effects in porous materials. In: Swartz, D.S., Shih, D.S., Evans, A.G., Wadley, H.N.G. (Eds.), Porous and Cellular Materials for Structural Applications. Materials Research Society Proceedings, vol. 521, Pittsburgh, PA, pp. 103–108.

Mukai, T., Kanahashi, H., Higashi, K., Yamada, Y., Shimojima, K., Mabuchi, M., Miyoshi, T., Nieh, T.G., 1999. Energy absorption of light-weight metallic foams under dynamic loading. In: Banhart, J., Ashby, M.F., Fleck, N.A. (Eds.), Cellular Metals and Metal Foaming Technology. Verlag MIT Publishing, Bremen, Germany, pp. 353–358.

Nesterenko, V.F., 2001. Dynamics of Heterogeneous Materials. Springer, New York.

Papka, S.D., Kyriakides, S., 1994. In-plane compressive response and crushing of honeycomb. J. Mech. Phys. Solids 42, 1499–1532.

Radford, D.D., Deshpande, V.S., Fleck, N.A., 2005. The use of metal foam projectiles to simulate shock loading on a structure. Int. J. Impact Eng. 31, 1152–1171.

Reid, S.R., Peng, C., 1997. Dynamic uniaxial crushing of wood. Int. J. Impact Eng. 19, 531–570.

Reid, S.R., Reddy, T.Y., Peng, C., 1993. Dynamic compression of cellular structures and materials. In: Jones, N., Wierzbicki, T. (Eds.), Structural Crashworthiness and Failure. Elsevier Applied Science Publishers, Amsterdam, pp. 295–340.

Ruan, D., Lu, G., Wang, B., Yu, T.X., 2003. In-plane dynamic crushing of honeycombs—a finite element study. Int. J. Impact Eng. 28, 161–182.

Shim, V.P.W., Tay, B.Y., Stronge, W.J., 1990. Dynamic crushing of strain softening cellular structures—a one-dimensional analysis. Trans. ASME J. Eng. Mater. Technol. 112, 398–405.

Skews, B.W., Atkins, M.D., Seitz, M.W., 1993. The impact of a shock wave on porous compressible foams. J. Fluid Mech. 253, 245–265.

Su, X.Y., Yu, T.X., Reid, S.R., 1995. Inertia-sensitive impact energy absorbing structures, Part I: Effects of inertia and elasticity. Int. J. Impact Eng. 16, 651–672.

Tan, P.J., Zou, Z., Li, S., Reid, S.R., Harrigan, J.J., 2005. On the mechanical properties of material with a densification regime, in preparation.

Wang, L., Labibes, K., Azari, Z., Pluvinage, G., 1994. Generalization of split Hopkinson pressure bar technique to use viscoelastic bars. Int. J. Impact Eng. 15, 669–686.